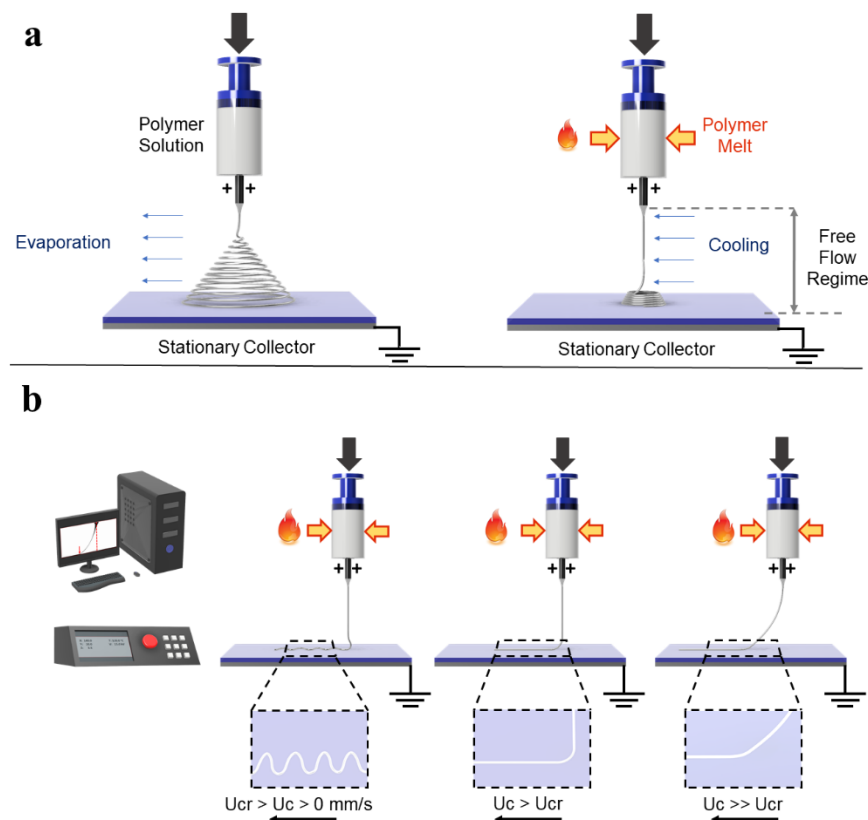
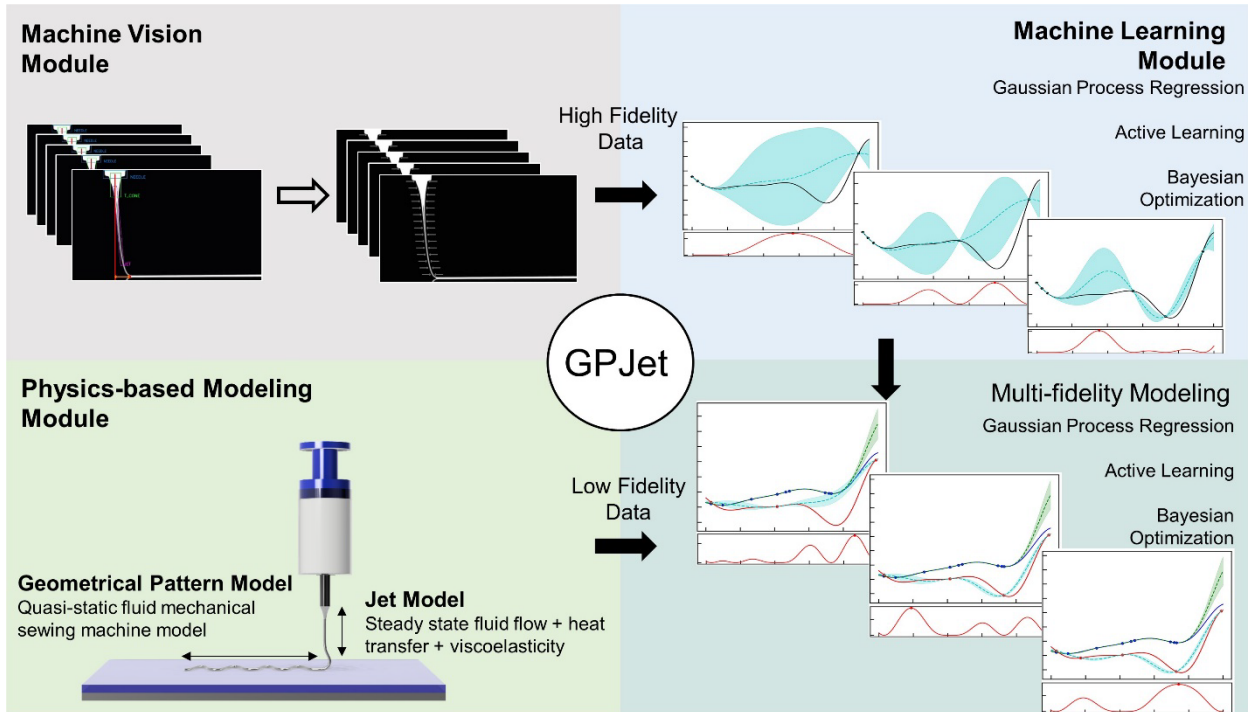


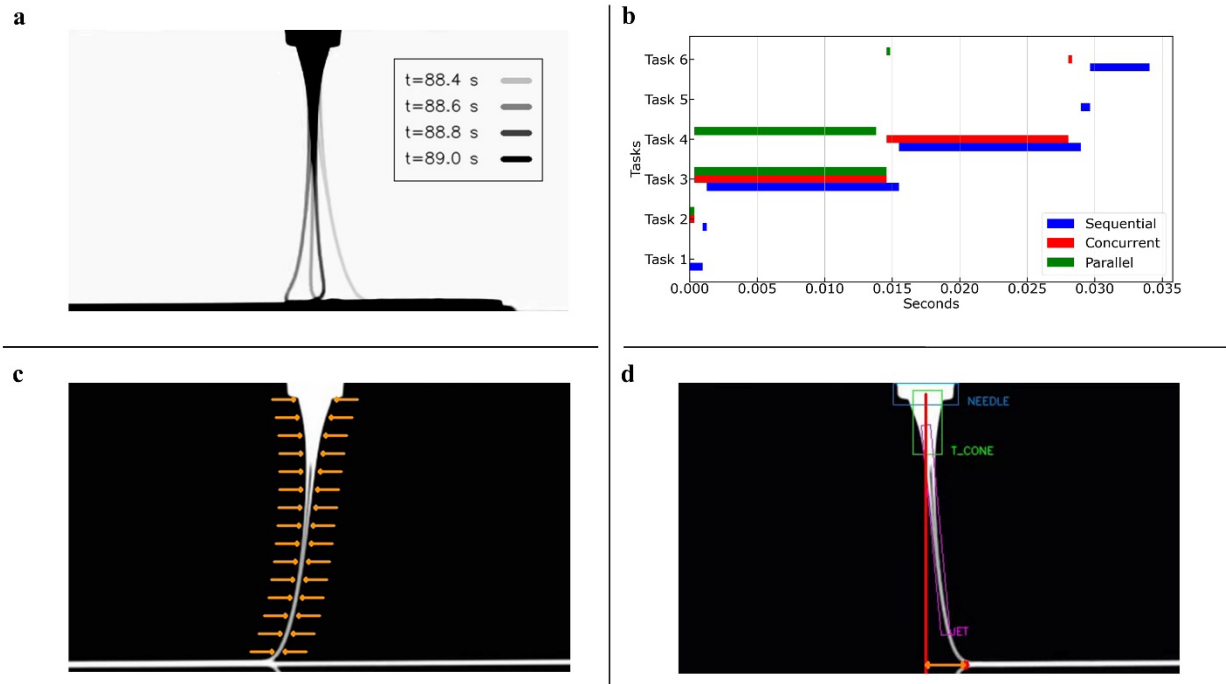
## Main Figures



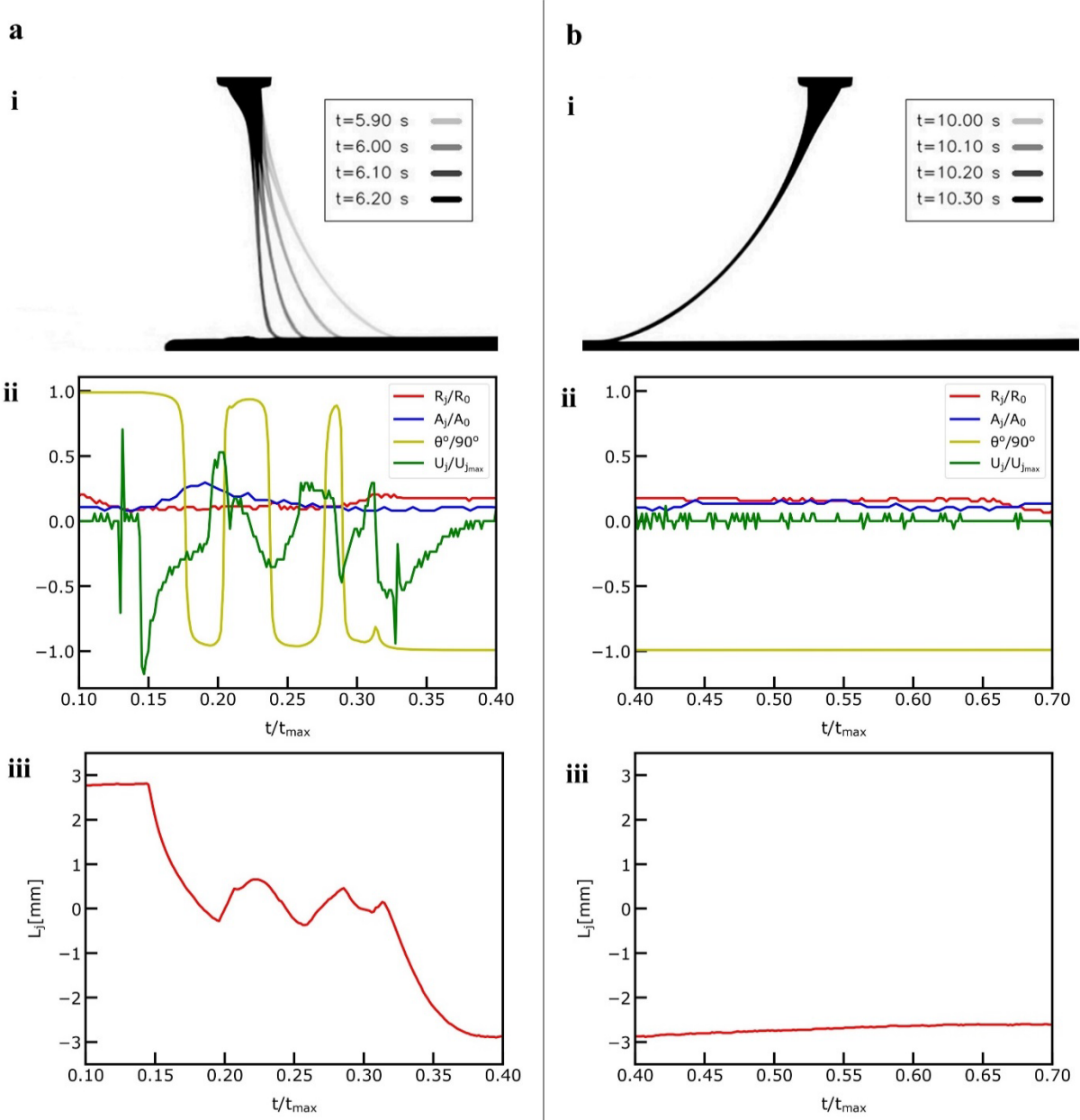
**Figure 1: Electrohydrodynamic Jet Printing Process.** Solution electrospinning (SES) vs. melt electrospinning (MES). The main differentiating feature between the two processes is the extent of the jet instabilities that arise from the electrostatic forces acting at the polymer jet-air interface. For MES, the chaotic jet regime is limited close to the grounded collector plate due to the high viscosity and dielectric properties of the pure polymer melt. b Direct melt electrowriting (MEW) and its operating principle.



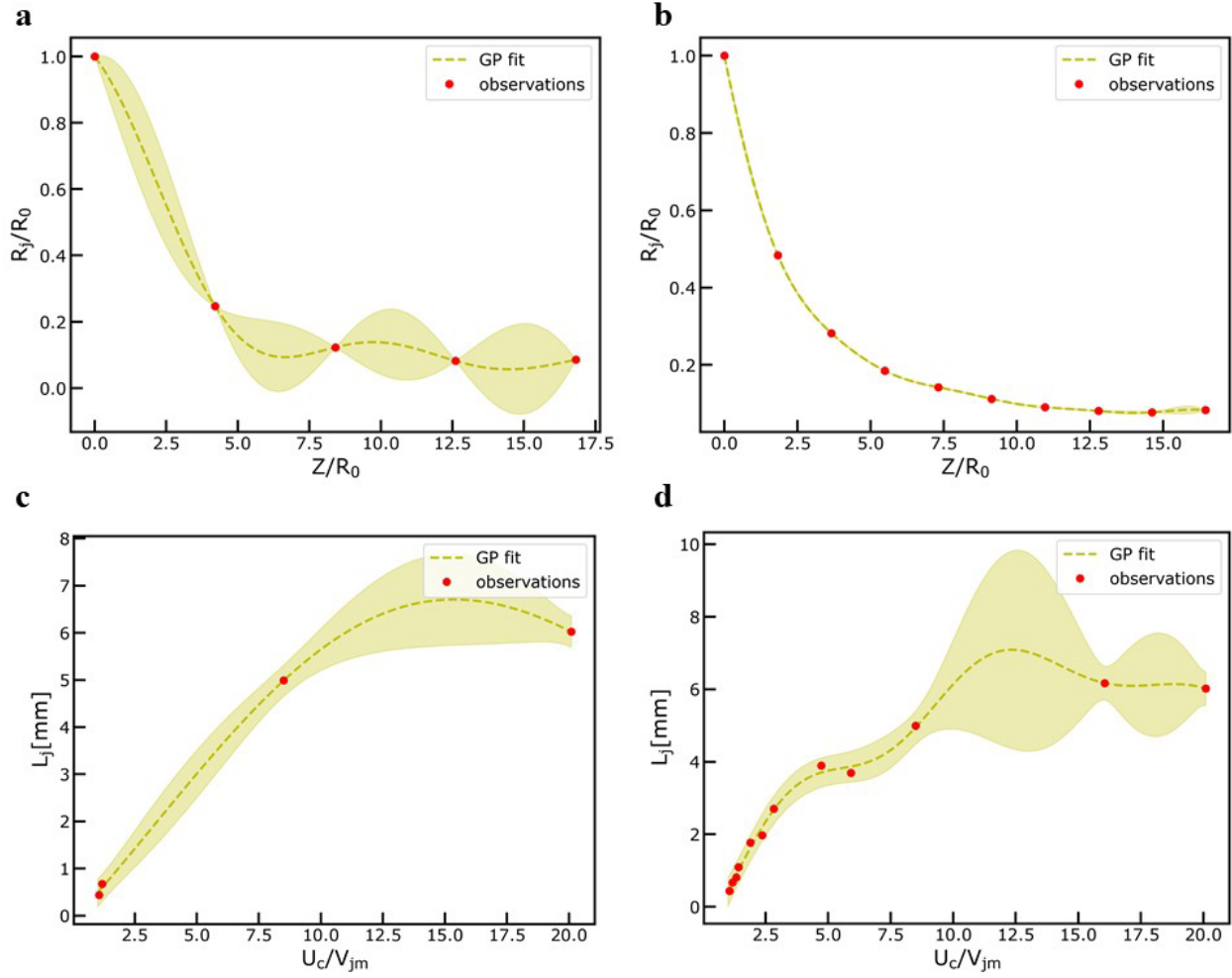
**Figure 2: The GPJet Pipeline Framework.** A Physics-informed Bayesian Machine Learning framework comprised by three different modules: a) the Machine Vision module, which takes as an input timeseries video focusing on the polymer jet in the free flow regime and performs extraction of high-fidelity jet features in real-time based on an automated image processing workflow b) the Physics-based Modeling Module, which and c) the Machine Learning module, which takes as an input high fidelity experimental data from the Machine Vision module and low fidelity modeling data from the and performs a series of data-driven tasks to learn the jet dynamics.



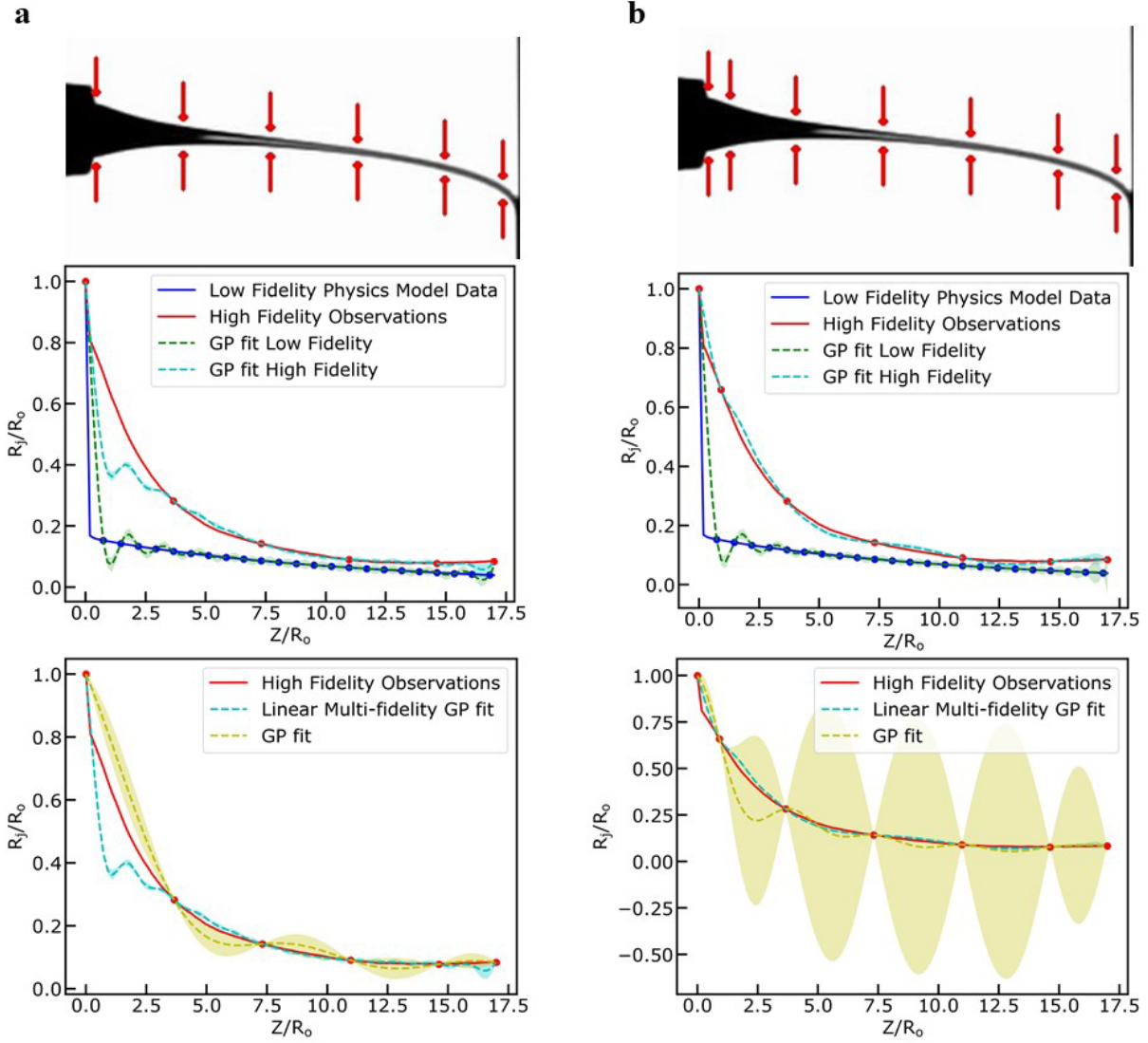
**Figure 3: Machine Vision Module.** **a)** Process dynamics and its scale. **b)** Profiling experiments for different code implementations. **c)** Edge-based feature extraction methodology (Task 3 in Figure 3b). **d)** Object-based feature extraction methodology (Task 4 in Figure 3b).



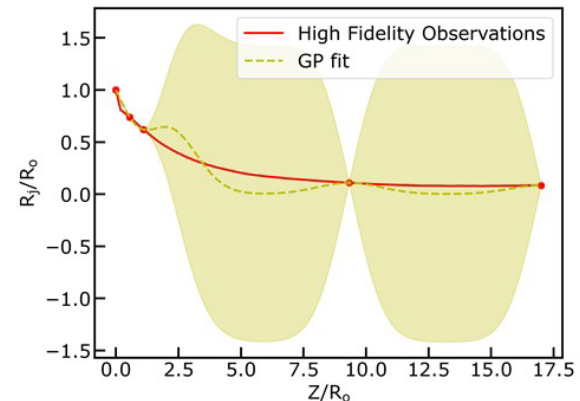
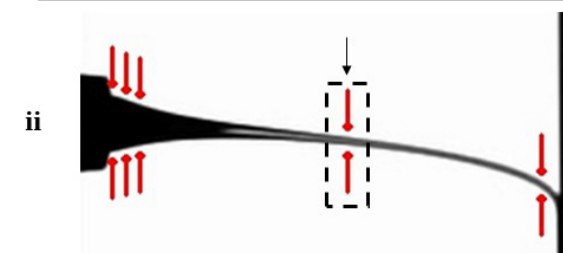
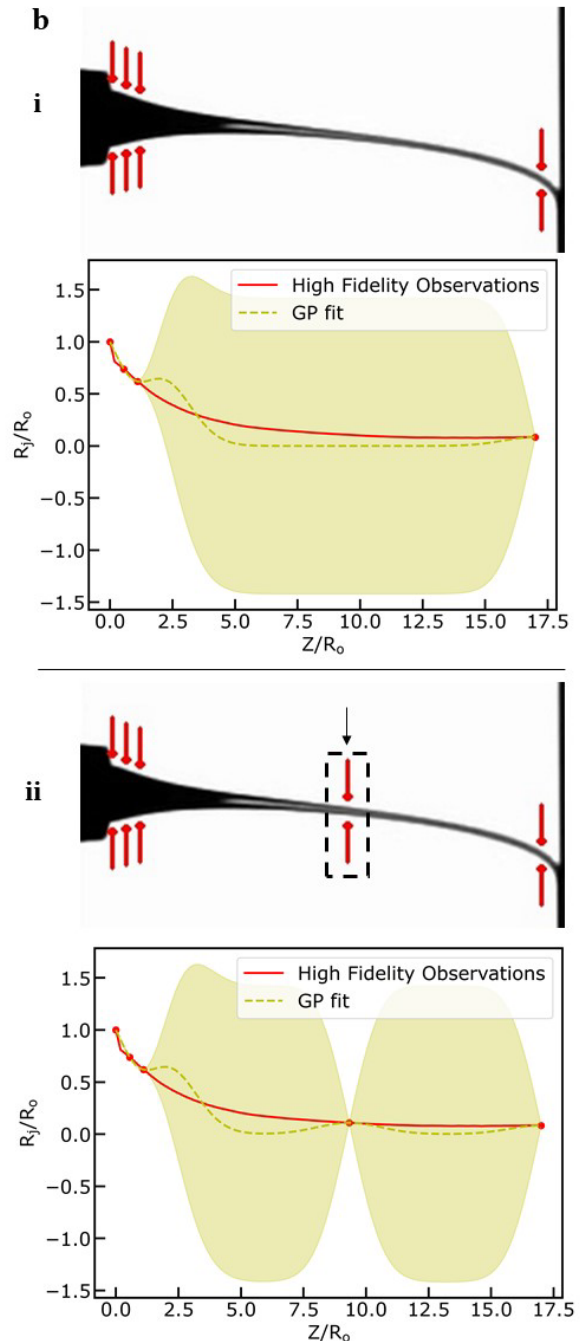
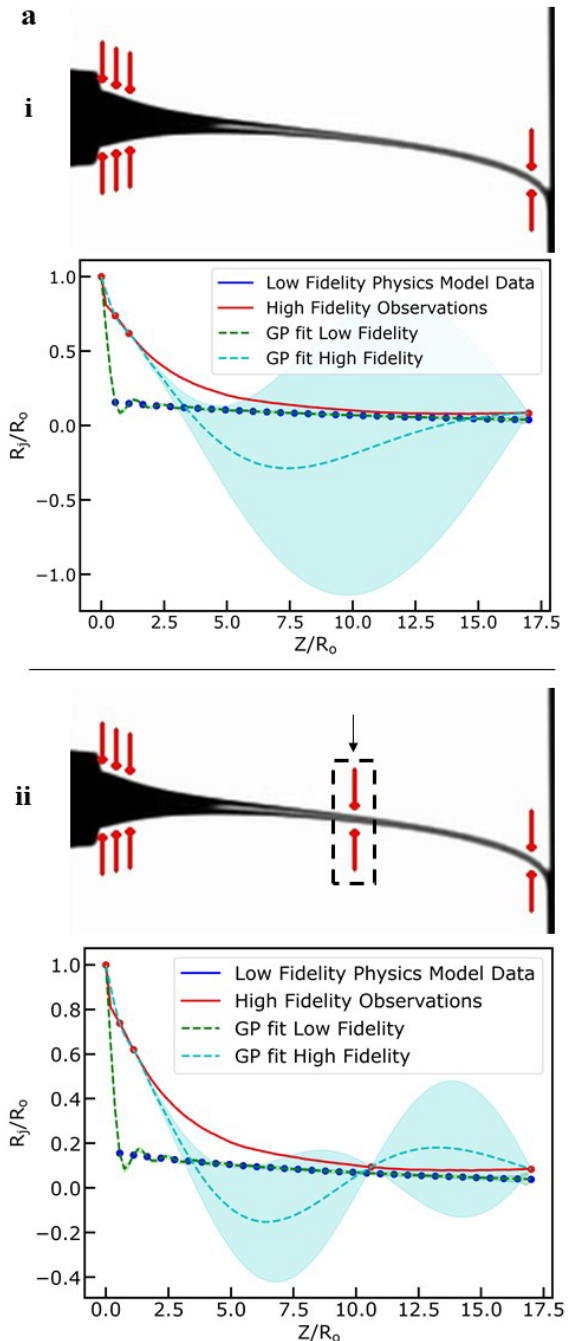
**Figure 4: Jet Metrology with the Machine Vision Module. a)** The extracted features during the deceleration-acceleration phase of the printing process. **i)** Overlaid video frames demonstrating the dynamics during the deceleration-acceleration phase and normalized jet length point of interest ( $Z/R_o = 17.5$ ) denoted with red color. **ii)** Normalized jet radius ( $R_j/R_o$ ), Normalized jet area ( $A_j/A_o$ ), Normalized jet angles ( $\theta^\circ/90^\circ$ ) and Normalized jet velocity ( $U_j/U_{j\max}$ ) at the denoted point of interest plotted against the normalized time ( $t/t_{max}$ ) during the deceleration-acceleration phase. **iii)** Jet lag distance ( $L_j$ ) plotted against the normalized time ( $t/t_{max}$ ) during the deceleration-acceleration phase. **b)** The extracted features during the steady speed phase pf the printing process. **i)** Overlaid video frames demonstrating the dynamics during the steady speed phase. **ii)** Normalized jet radius ( $R_j/R_o$ ), Normalized jet area ( $A_j/A_o$ ), Normalized jet angles ( $\theta^\circ/90^\circ$ ) and Normalized jet velocity ( $U_j/U_{j\max}$ ) at the denoted point of interest plotted against the normalized time ( $t/t_{max}$ ) during the steady speed phase. **iii)** Jet lag distance ( $L_j$ ) plotted against the normalized time ( $t/t_{max}$ ) during the steady speed phase.

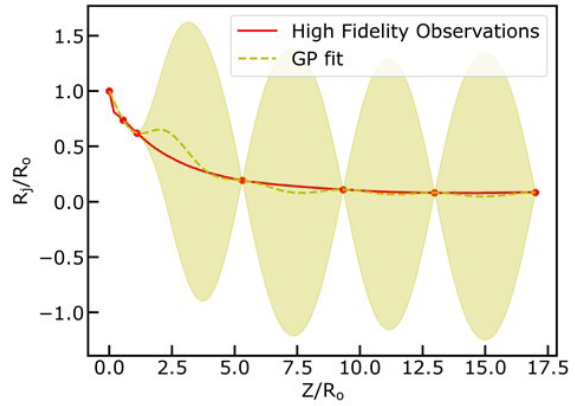
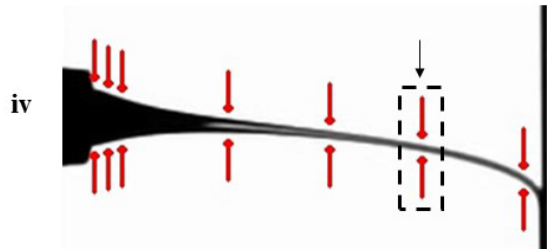
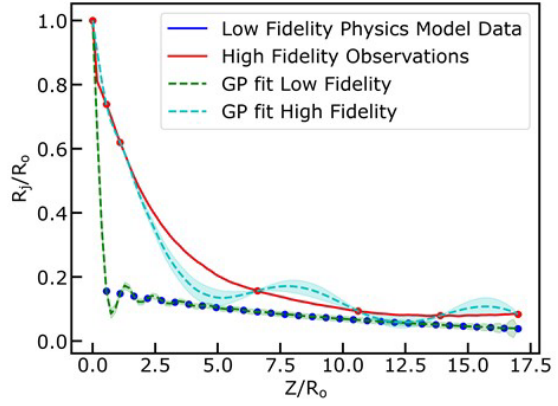
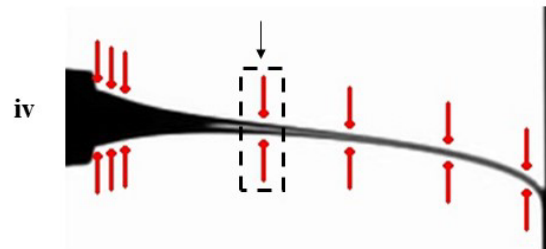
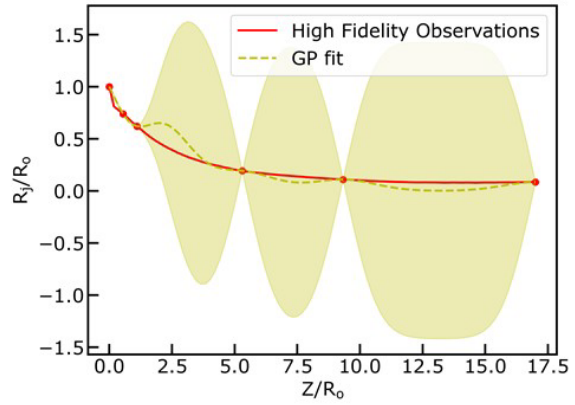
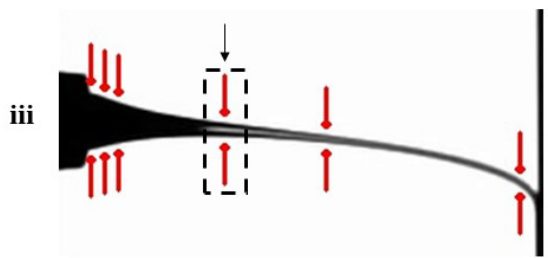
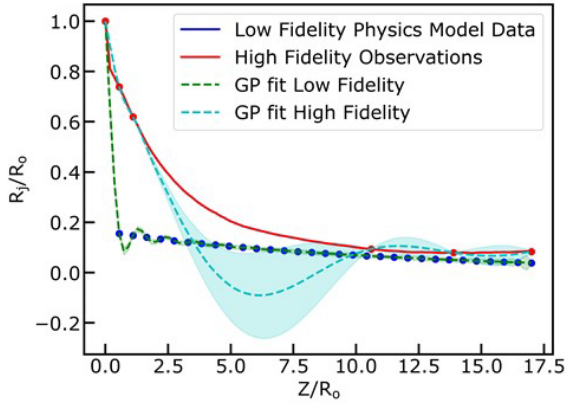
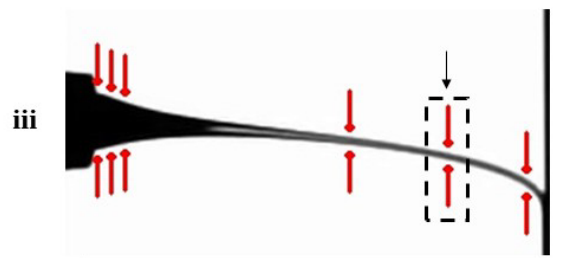


**Figure 5: Results of Gaussian Process Modeling Regression Tasks.** **a)** fitting normalized ( $R_j/R_0$ ) jet radius observation data ( $n=5$ ) obtained from the computer vision metrology module of the GPJet framework at specific z axis coordinates along the normalized jet length ( $Z/R_0$ ). **b)** fitting normalized jet radius using a higher number of observation data ( $n=10$ ) compared to the previous case (a). **c)** fitting lag distance ( $L_j$ ) observation data ( $n=3$ ) obtained from the computer vision metrology module of the GPJet framework for specific speed ratios ( $U_c/V_{jm}$ ). **d)** fitting lag distance using all available observation data ( $n=12$ ). For non-normalized quantities units are in SI. Filled contours represent uncertainty bounds (95% confidence intervals (CIs)).



**Figure 6: Results of Multi-fidelity Modeling Regression Tasks.** **a)** fitting normalized high fidelity observation data ( $n=6$ , red color) of jet radius ( $R_j/R_o$ ) and low fidelity model data obtained from the computer vision metrology module of the GPJet framework and from the multi-physics model, respectively, at specific z axis coordinates along the normalized jet length ( $Z/R_o$ ) and comparing the results with a simple GP fit using the same number of high fidelity observation data. **b)** fitting a higher number of normalized high fidelity observation data ( $n=7$ , red color) of jet radius ( $R_j/R_o$ ) and low fidelity model data obtained from the computer vision metrology module of the GPJet framework and from the multi-physics model, respectively, at specific z axis coordinates along the normalized jet length ( $Z/R_o$ ) and comparing the results with a simple GP fit using the same number of high fidelity observation data.





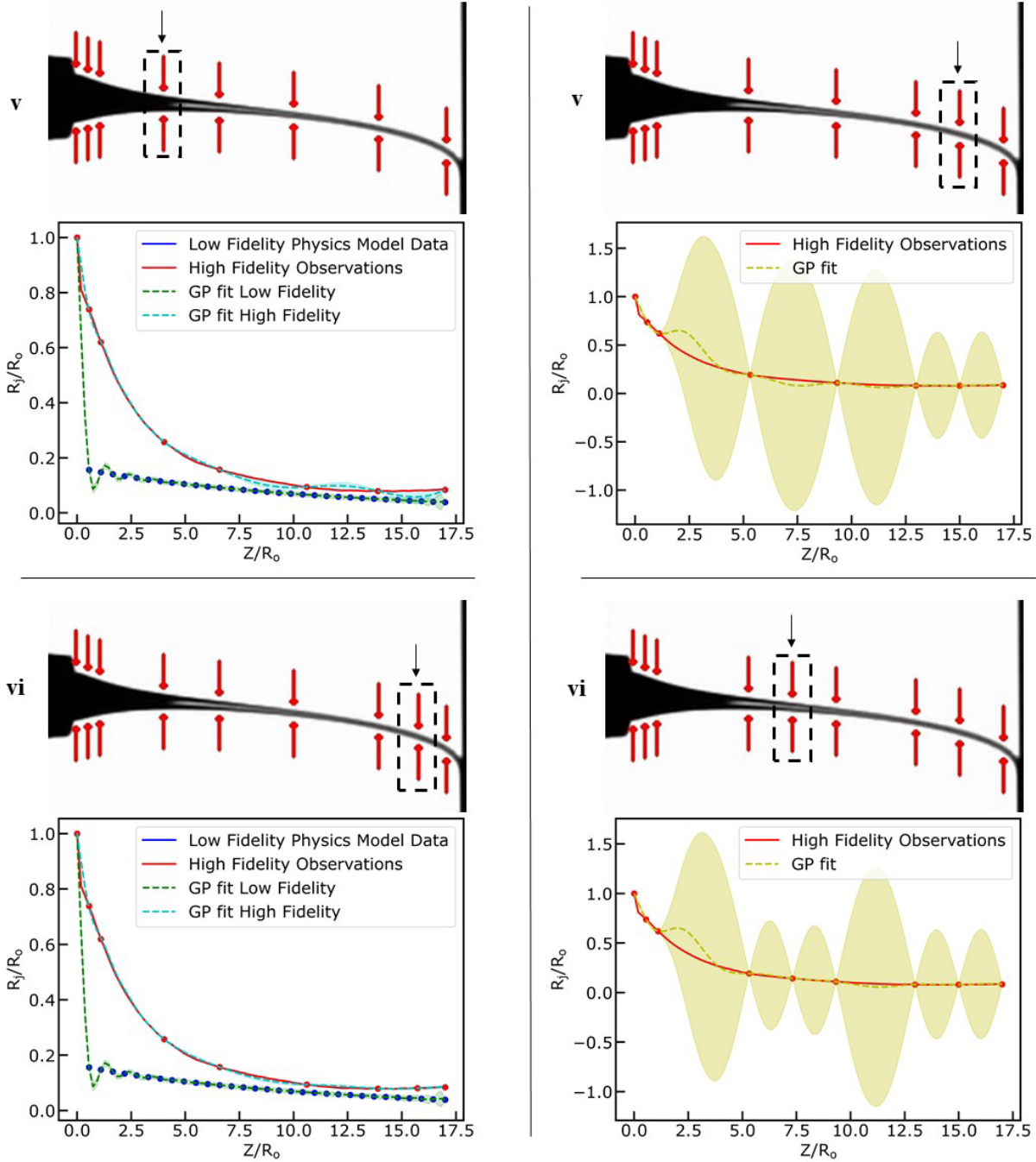


**Figure 7: Results of Active Learning process on Multifidelity Modeling Task.** **a)** exploring the design space using Active Learning to fit a Multifidelity Gaussian Process to normalized high fidelity observation data (red color) of jet radius ( $R_j/R_o$ ) and low fidelity model data obtained from the computer vision metrology module of the GPJet framework and from the multi-physics model, respectively, at specific z axis coordinates along the normalized jet length ( $Z/R_o$ ) (**i – vi** denote the iterations of the active learning algorithm until it meets its termination criteria). **B)** exploring the design space using Active Learning to fit a Gaussian Process to normalized high fidelity observation data (red color) of jet radius ( $R_j/R_o$ ) obtained from the computer vision metrology module of the GPJet framework at specific z axis coordinates along the normalized jet length ( $Z/R_o$ ) (**i – vi** denote the iterations of the active learning algorithm until it meets its termination criteria).

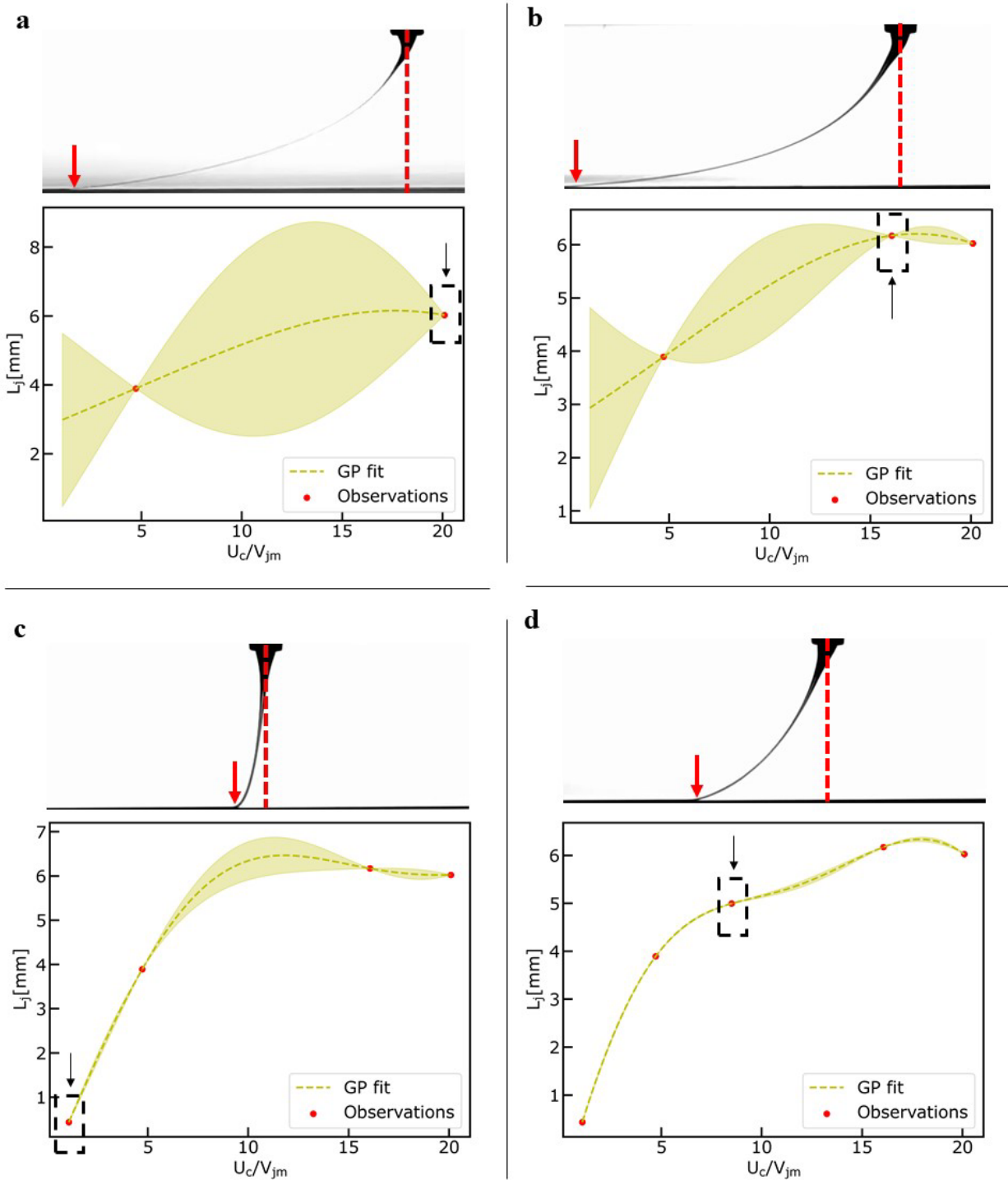


**Figure 8: Results of Exploring the Design Space Task.** Exploring the design space using active learning to fit a Gaussian Process Model to lag distance ( $L_j$ ) observation data obtained from the computer vision metrology module of the GPJet framework for specific speed ratios ( $U_c/V_{jm}$ ). **a-d)** Iterations of the active learning algorithm until it meets termination criteria.

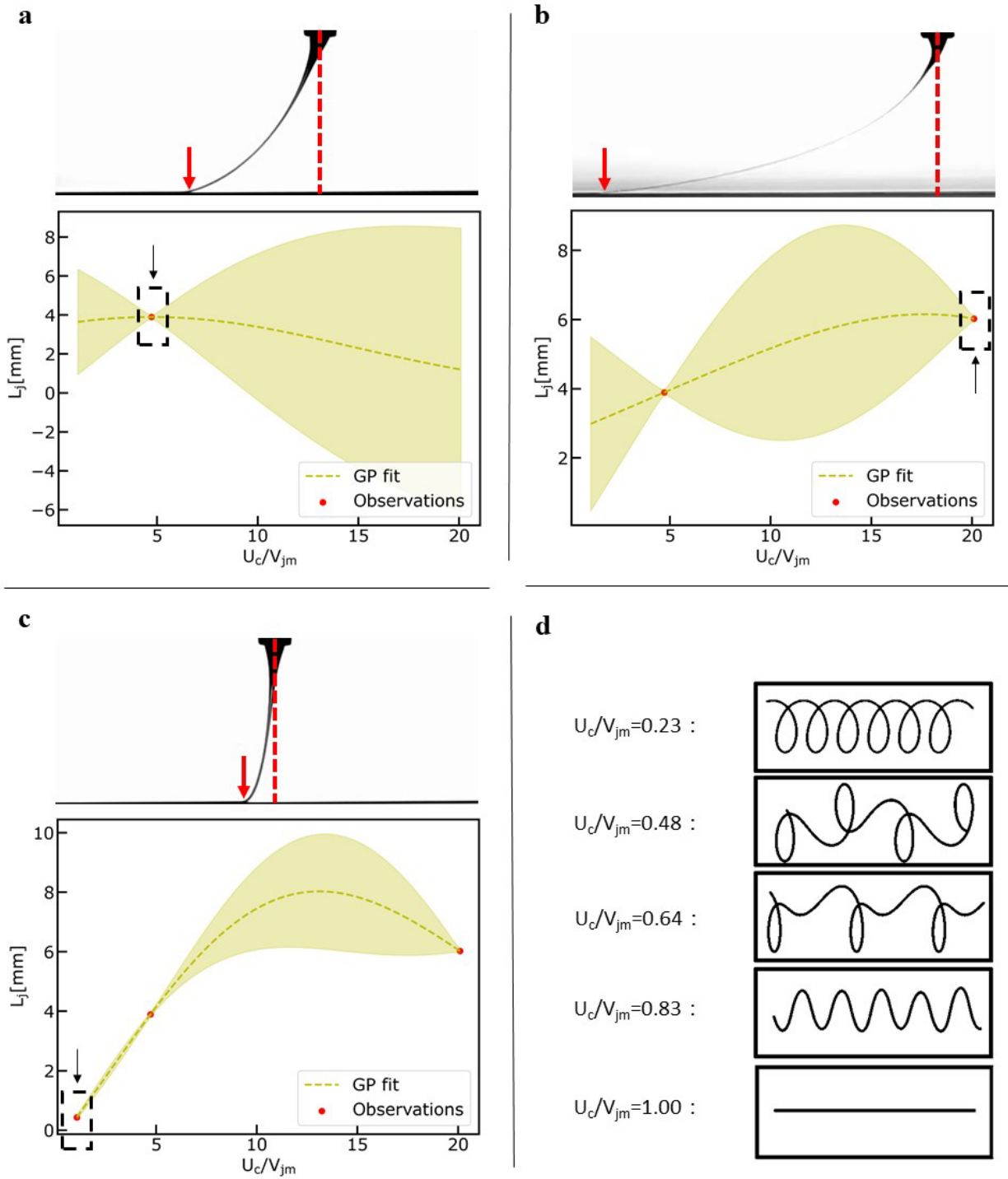


**Figure 9: Results of Bayesian Optimization Task.** Performing Bayesian Optimization to find the minimum lag-distance ( $L_j$ ) by fitting a Gaussian Process Model to lag distance ( $L_j$ ) observation data obtained from the computer vision metrology module of the GPJet framework for specific speed ratios ( $U_c/V_{jm}$ ). **a-c**) Iterations of the Bayesian optimization algorithm until it meets termination criteria. **d)** For speed ratios less than one ( $U_c/V_{jm} < 1$ ) the process is unstable, no straight line is formed, instead the translated coiling, alternating loops, W patterns and meanders patterns are formed, therefore no lag distance ( $L_j$ ) observation data can be obtained from the computer vision metrology module of the GPJet framework.